



THE UNIVERSITY *of* EDINBURGH

Edinburgh Research Explorer

Structural and electronic properties of the alkali metal incommensurate phases

Citation for published version:

Woolman, G, Naden Robinson, V, Marqués, M, Loa, I, Ackland, GJ & Hermann, A 2018, 'Structural and electronic properties of the alkali metal incommensurate phases', *Physical Review Materials*, vol. 2, no. 5, 053604. <https://doi.org/10.1103/PhysRevMaterials.2.053604>

Digital Object Identifier (DOI):

[10.1103/PhysRevMaterials.2.053604](https://doi.org/10.1103/PhysRevMaterials.2.053604)

Link:

[Link to publication record in Edinburgh Research Explorer](#)

Document Version:

Publisher's PDF, also known as Version of record

Published In:

Physical Review Materials

General rights

Copyright for the publications made accessible via the Edinburgh Research Explorer is retained by the author(s) and / or other copyright owners and it is a condition of accessing these publications that users recognise and abide by the legal requirements associated with these rights.

Take down policy

The University of Edinburgh has made every reasonable effort to ensure that Edinburgh Research Explorer content complies with UK legislation. If you believe that the public display of this file breaches copyright please contact openaccess@ed.ac.uk providing details, and we will remove access to the work immediately and investigate your claim.



Structural and electronic properties of the alkali metal incommensurate phases

Gavin Woolman, Victor Naden Robinson, Miriam Marqués, Ingo Loa, Graeme J. Ackland, and Andreas Hermann*

Centre for Science at Extreme Conditions, School of Physics and Astronomy and SUPA, The University of Edinburgh, Edinburgh EH9 3FD, United Kingdom

(Received 27 February 2018; published 11 May 2018)

Under pressure, the alkali elements sodium, potassium, and rubidium adopt nonperiodic structures based on two incommensurate interpenetrating lattices. While all elements form the same “host” lattice, their “guest” lattices are all distinct. The physical mechanism that stabilizes these phases is not known, and detailed calculations are challenging due to the incommensurability of the lattices. Using a series of commensurate approximant structures, we tackle this issue using density functional theory calculations. In Na and K, the calculations prove accurate enough to reproduce not only the stability of the host-guest phases, but also the complicated pressure dependence of the host-guest ratio and the two guest-lattice transitions. We find Rb-IV to be metastable at all pressures, and suggest it is a high-temperature phase. The electronic structure of these materials is unique: they exhibit two distinct, coexisting types of electride behavior, with both fully localized pseudoanions and electrons localized in 1D wells in the host lattice, leading to low conductivity. While all phases feature pseudogaps in the electronic density of states, the perturbative free-electron picture applies to Na, but not to K and Rb, due to significant *d*-orbital population in the latter.

DOI: [10.1103/PhysRevMaterials.2.053604](https://doi.org/10.1103/PhysRevMaterials.2.053604)

I. INTRODUCTION

The crystalline solids of the group-I (alkali) elements at standard temperature and pressure conditions are exceedingly simple: they all adopt a body-centered-cubic (bcc) structure, and their single valence electron is quasifree, so that the band structure and Fermi surface are not perturbed much from that of a homogeneous electron gas. It was once assumed that upon compression the alkali metals should retain their free-electron-like behavior, while possibly adopting more close-packed structures. Indeed, all alkalis exhibit a phase transition to a close-packed face-centered cubic (fcc) phase under modest compression, see Table I. But compressing further results in a marked departure from this simple picture, and all alkali elements exhibit complex crystal structures demonstrated in a succession of experiments [1–16]. These experiments were accompanied with calculations showing intriguing electronic features including electride behavior (the localization of electrons in interstitial lattice sites) and reconstructions to match the Brillouin zone to the Fermi surface [17–21].

One particularly intriguing feature is the emergence of *incommensurate* phases, i.e., elemental crystal structures where some of the atoms form a “host” lattice, inside which reside “guest” atoms, which themselves form a regular crystal structure. The host lattice has channels (by convention defined along the *c* axis) occupied by chains of the guest atoms, see Fig. 1. The guest atoms form a lattice with lattice parameter c_G that need not be commensurate with the host lattice parameter c_H . As a result, the crystal is biperiodic along the *c* direction and can be described crystallographically using four-dimensional superspace groups [22]. Various explanations on what makes

these incommensurate structures stable have been put forward, including electron localization, *s-d* electron transfer or hybridization [15], a preference for 9–10 bonded neighbors [18,23], Fermi surface-Brillouin zone effects [24,25], and the high entropy, which leads to the so-called “chain melting” [26].

Sodium, potassium, and rubidium have all been observed to form incommensurate structures under pressure. They all share the same tetragonal host structure of *I4/mcm* space group symmetry with 16 atoms in the conventional unit cell. The guest structures differ for each element, and are described in more detail below.

Sodium. The electrical conductivity of sodium is highly pressure dependent, and at pressures above 180 GPa it forms an insulating phase [16]. This remarkable transition is associated with electronic charge becoming localized in interstitial regions [15,16,27]. This so-called “electride” phase is preceded by a series of phase transitions away from simple close-packing, through a variety of low-symmetry phases. Between 100 and 105 GPa, fcc-Na transforms into the *cI16* phase, a distorted bcc variant, which also heralds a minimum in the melting curve at about 300 K [11,28]. This structure was shown to be associated with Fermi-surface Brillouin-zone interactions [19] and has also been associated with an *s-p* transition of the valence electrons [16,29].

Sodium’s incommensurate phase, Na-V, is stable at room temperature between 125 and 180 GPa, between the poorly conducting *oP8* Na-IV and the optically transparent electride *hP4* Na-VI [11,14–16,29,30]. It has a monoclinic guest lattice (see Fig. 1), and is sometimes called Na-*tI19*, because there are roughly three guest atoms for every 16 host atoms. Lazicki *et al.* commented on charge gathering in “periodically modulated columns along *z*” [15], an effect also noticed in calculations of Rb-IV (see below) [31].

*a.hermann@ed.ac.uk

TABLE I. The experimental room-temperature high-pressure phase evolution of the alkali metals. For Na, K, and Rb the second set of numbers indicate transition pressures from our ground state calculations (all in GPa). “h-g” labels the occurrences of incommensurate host-guest phases. Adapted from [13,19,20].

Li	bcc	$\xrightarrow{7.5}$	fcc	$\xrightarrow{39}$	<i>hR1</i>	$\xrightarrow{42}$	<i>cI16</i>	$\xrightarrow{60}$	<i>oC88</i>	$\xrightarrow{65}$	<i>oC40</i>	$\xrightarrow{95}$	<i>oC24</i>
Na	bcc	$\xrightarrow{65/80}$	fcc	$\xrightarrow{104/124}$	<i>cI16</i>	$\xrightarrow{117/x}$	<i>oP8</i>	$\xrightarrow{125/153}$	h-g	$\xrightarrow{180}$	<i>hP4</i>		
K	bcc	$\xrightarrow{11.6/11}$	fcc	$\xrightarrow{20/17.5}$	h-g	$\xrightarrow{54/39}$	<i>oP8</i>	$\xrightarrow{90/51}$	<i>tI4</i>	$\xrightarrow{96/96}$	<i>oC16</i>		
Rb	bcc	$\xrightarrow{7/6}$	fcc	$\xrightarrow{13/14}$	<i>oC52</i>	$\xrightarrow{17/x}$	h-g	$\xrightarrow{20/16}$	<i>tI4</i>	$\xrightarrow{48/42}$	<i>oC16</i>		
Cs	bcc	$\xrightarrow{2.4}$	fcc	$\xrightarrow{4.2}$	<i>oC84</i>	$\xrightarrow{4.3}$	<i>tI4</i>	$\xrightarrow{12}$	<i>oC16</i>	$\xrightarrow{72}$	dhcp		

Potassium. Incommensurate potassium K-III was first described by McMahon *et al.* [10]. It is, at room temperature, followed by the *oP8* phase at 54 GPa [32].

The guest structure of potassium has three distinct phases [9]. At 23–30 GPa, K-IIIa has a primitive tetragonal guest lattice (space group *P4/mmm*). At pressures above 30 GPa, atoms in adjacent guest chains are displaced by $1/2 c_G$ such

that the guest structure has an A-centered tetragonal lattice (space group *Ammm*) with a doubled unit cell (K-IIIb, see Fig. 1). Above 39.7 GPa, the guest structure transforms back to that of the K-IIIa structure. The ratio of the lattice parameters c_H/c_G against pressure is continuous through the IIIa-IIIb-IIIa transitions, and exhibits a minimum at 30 GPa. A hexagonal *hP4* phase has been observed in some potassium samples between 25 and 35 GPa, a range usually associated with incommensurate K-III [5]. It is not known which is the true ground state.

The guest lattice of K-III has been observed by McBride *et al.* to lose long range order between chains upon heating [26]. There is a transition temperature above which correlations between the guest atom chains in adjacent channels are lost. This so-called chain-melting temperature depends on pressure and changes at the phase boundary between K-IIIa and K-IIIb. McBride *et al.* confirmed the local minimum in the c_H/c_G ratio as a function of pressure. They also reported a sharp increase in the slope of the melt line beyond the KIIIa-KIIIb-liquid triple point, however, this implies a large change in density between KIIIa-KIIIb, which was not seen in diffraction data.

Rubidium. The incommensurate structure of Rb-IV is only seen over a comparatively small pressure range of ≈ 16 –20 GPa in room-temperature experiments [33]. In this structure, the guest atoms form a body-centered tetragonal lattice [6]. The guest atoms in Rb-IV are displaced by $1/2 c_G$ between adjacent guest chains, but in a different arrangement than for K-IIIb, see Fig. 1.

X-ray studies have shown “chain melting” in Rb at the lower end of Rb-IV’s stability range, below 16.7 GPa at room temperature [8], which could be due to loss of order between chains. Experiments by Loa *et al.* between 16.3 and 18.4 GPa observed two well-defined longitudinal acoustic phonon branches along the *c* axis direction, corresponding to separate oscillations from the host lattice and guest chains [34]. They found the measured sound velocity of the guest chain oscillations could be well predicted by treating the guest atoms as a linear monatomic chain suggesting that the “melting” is due to loss of order between chains.

Across the alkali metals, similarities and subtle differences emerge between the various incommensurate phases. In each case, they appear in an intermediate pressure regime, where they compete for stability with complex electride phases such as *oP8*, *hP4*, or *oC52*. In all cases, the host structure is the same. In contrast, their guest structures are all different, as is the evolution of the host-guest ratio as function of pressure.

In general, these structures pose a challenge to computational studies, since commensurate unit cells need to be used

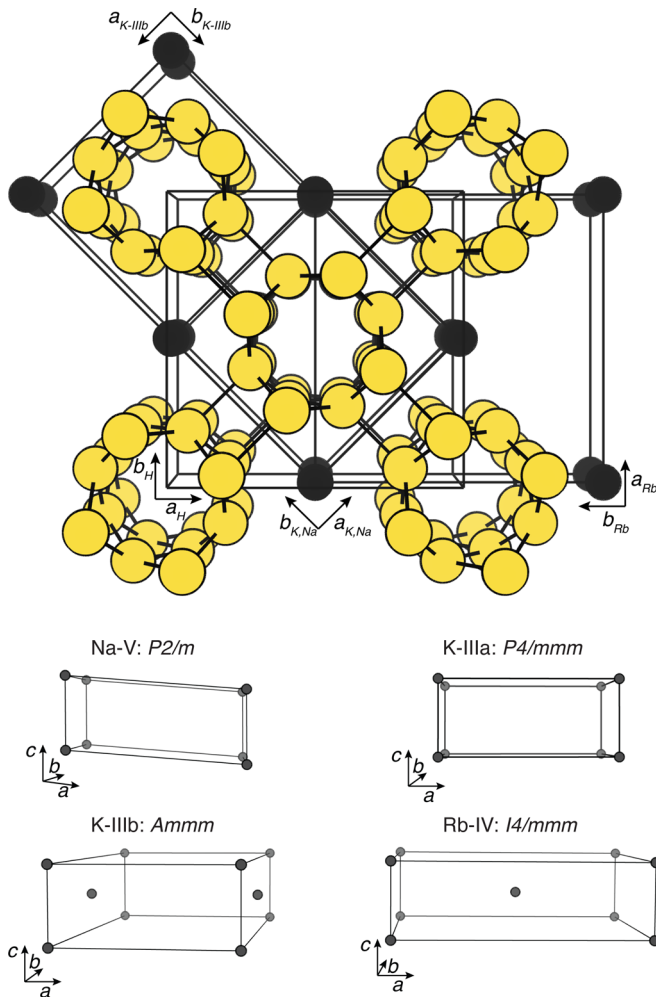


FIG. 1. Incommensurate structures of the alkali metals, host/guest atoms are indicated by yellow/black circles. (Top) The tetragonal host lattice unit cell common to all elements, seen along the *c* axis. (Bottom) The four different guest unit cells seen in various elements; the space group and atomic positions are indicated, the (*a*, *b*) axes are rotated relative to the upper panel, as indicated therein.

as approximants that should have c_H/c_G ratios close to those seen in nature. Previous computational studies have usually relied on the smallest possible commensurate approximants, although examples exist, for elementary and compound incommensurates, where the role of different host-guest ratios has been explored [35–39].

In this work, we present a comparative analysis of the incommensurate phases in the alkali metals from electronic structure calculations. We assess the ability of density functional theory to describe the phase sequence in each of sodium, potassium, and rubidium, and study the role of the different guest structures and choice of approximants for the incommensurate phases. We are able to predict (in case of sodium) and confirm (in K and Rb) the pressure evolution of the host-guest ratio c_H/c_G , and analyze in detail the electronic structure of each phase.

II. COMPUTATIONAL METHODOLOGY

Total energy calculations were carried out within the framework of density functional theory as implemented in the CASTEP code [40]. Due to being well tested for the alkali elements [41–43] the PBE and PBEsol exchange-correlation functionals were used to describe effective electron-electron interactions. Constant-pressure structural optimizations employed a quasi-Newton geometry optimization scheme [44].

For each element, the pseudopotential and plane wave cutoff energy were kept constant across structures so that calculated enthalpies could be compared. Ultrasoft pseudopotentials [45] were generated on the fly at the start of each calculation. Including the filled $(n-1)sp$ electron shell immediately below the outer ns valence electron in the valence space is necessary to correctly describe the alkalis at densities where these inner electron wavefunctions begin to overlap [31]. Hence, we used $\text{Na}(2s^2 2p^6 3s^1)$, $\text{K}(3s^2 3p^6 4s^1)$, and $\text{Rb}(4s^2 4p^6 5s^1)$ valence spaces, with cutoff radii of 1.8, 1.7, and 2.1 bohrs, respectively. Plane wave cutoffs were set to 500, 400, and 300 eV, respectively, and Brillouin zone sampling was done on regular k -point grids with separations of 0.02 \AA^{-1} . These settings ensured converged energy differences between the relevant phases.

Initial crystal structures of all standard (commensurate) phases were obtained from the Inorganic Crystal Structure Database (ICSD) [46]. For the incommensurate phases (see Fig. 2) approximants were constructed by using the host structure shown in Fig. 1 as the starting point. Supercells of this lattice along the c axis were then created into which guest atoms were placed at the relevant positions (a $\sqrt{2} \times \sqrt{2}$ unit cell of the host structure in the ab plane is required for the K-IIIb guest structure). This procedure results in unit cells for a series of commensurate ratios c_H/c_G , which were chosen to cover the respective experimental range while ensuring computational feasibility. We will use the notation ng/mh to denote a commensurate unit cell with n guest lattice unit cells and m host lattice unit cells along c ; this is equivalent to a host-guest ratio $c_H/c_G = n/m$. The approximants we used included 4g/3h (56 atoms per unit cell for K-IIIa and Rb-IV), 3g/2h (38 atoms), 8g/5h (96 atoms), 5g/3h (58 atoms), 7g/4h (78 atoms), 9g/5h (98 atoms) and 2g/1h (20 atoms); unit cells with the K-IIIb guest structure are twice as large.

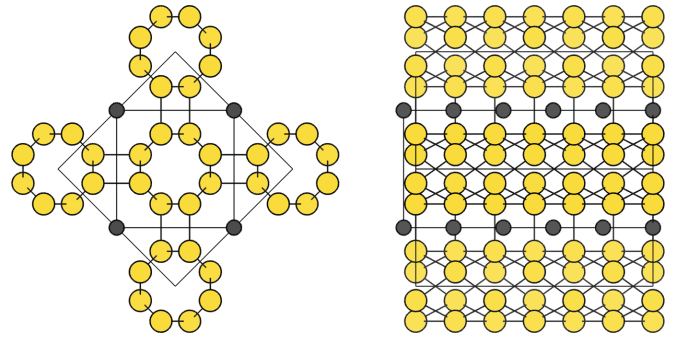


FIG. 2. The K-IIIa structure as seen in experiment at 27.7 GPa, along the [001] (left) and the $[1\bar{1}0]$ directions (right) [9]. Host/guest atoms are denoted by yellow/black spheres. Side view shows multiples of host (x3) and guest unit cells (x5) along the c axis; the incommensurate nature of the two sub-lattices is evident.

The guest atom positions for Na-V, K-IIIa and -IIIb, and Rb-IV were created according to the guest unit cells given in the experimental structure determination [6,9,30]. In Na-V, the guest unit cell is monoclinic ($\beta = 94.7^\circ$ at 147 GPa). Modelling such a guest lattice would require the creation of very large commensurate approximants along the a axis, which is currently not feasible to be studied computationally. Therefore we created Na-V approximants with tetragonal guest lattices, and allowed neighboring guest chains to move relative to one another. This allowed examination of any consistent offset between neighboring guest chains, including the body-centered form seen in Rb-IV (Fig. 1).

To understand the electronic structure of the incommensurates we follow a twofold approach. Firstly, the electronic wave functions are projected onto spherical harmonics. Population analyses based on this partition of the Hilbert space hold little physical meaning as they are highly dependent on the original basis set used for the calculation. Moreover, these basis sets are atom-centered and can fail to account for electrons localized in interstitial regions. Therefore their meaning for metals must be interpreted more as indicating relative charge density in the neighborhood of each atom rather than closely bound partial charge. However, examining their relative values can be a useful indicator of charge displacement and can be compared across structures provided consistent choice of basis set (i.e., consistent pseudopotential, plane-wave cutoff, k -point grid, etc.) [47,48]. Secondly, we performed topological analysis of the electron density and the electron localization function (ELF [49,50]) with the CRITIC2 code [51] for a deeper insight into the chemical bonding and the localization patterns. These real-space scalar fields are obtained with the VASP code in conjunction with “hard” projector-augmented wave (PAW) frozen core data sets [52,53]. The topological analysis first identifies the critical points of the scalar fields, i.e., points where their gradient vanishes. These are then classified as maxima, first-order saddle points, second-order saddle points, or minima. The maxima of the electron density are usually located at the nuclei (electrides are notable exceptions), while its first-order saddle points correspond to chemical bonds (denoted bond critical points) within the quantum theory of atoms in molecules [54,55]. The electron density and its Laplacian at these points are used to characterize the bond

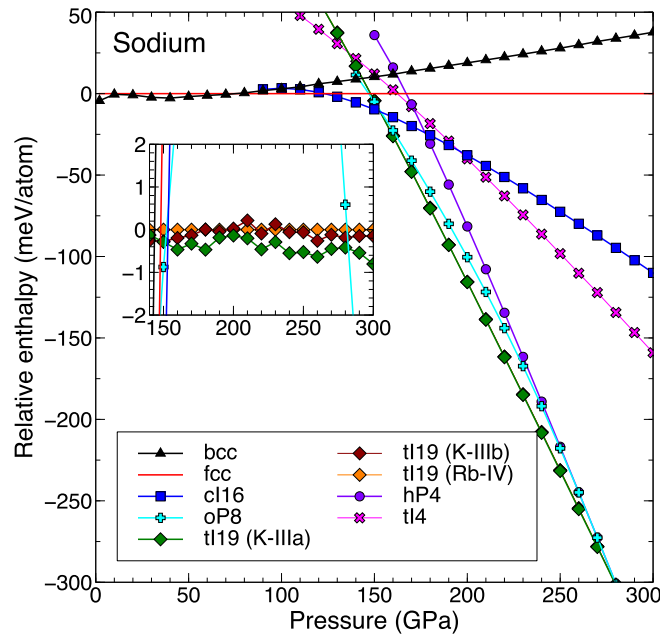


FIG. 3. Sodium formation enthalpies per atom with respect to the fcc structure, from PBE calculations. For all *tI19* structures, the enthalpy at the optimal host-guest ratio at every pressure is shown. Inset shows pressure region 140–300 GPa, relative to the Rb-IV-type guest structure of *tI19*.

strengths and their character. The unit cell is unambiguously partitioned into topological atoms, defined by the union of the electron density maxima with their attraction basins and delimited by zero-flux surfaces. An equivalent partition of space based on the ELF also yields nonoverlapping basins with well-defined chemical interpretations: atomic shells, covalent bonds, and lone pairs. By definition, ELF is a relative measure of the electron localization with respect to the homogeneous electron gas (HEG) and its values are bound between 0 and 1, with 0.5 the value of the HEG. ELF commonly exhibits maxima and, in general, approaches 1 in the regions of space where electron pairing occurs. We studied here not only the distribution of ELF maxima (ELF attractors) but also its first-order saddle points (called bond interaction points), which can be used to establish connectivity between ELF basins and to characterize the chemical bonding. A useful index proposed by Silvi and Gatti for measuring the delocalization within a metallic structure, the so-called localization window, is defined as the difference between the ELF values at a valence maximum and at the bond interaction points bounding its attraction basin [56].

III. ENTHALPIES AND STRUCTURES

Sodium. For sodium, the calculated relative enthalpies of formation of various phases as a function of pressure are shown in Fig. 3. Full crystallographic information for all phases discussed for all elements can be found in Ref. [57]. At 1 atm, the bcc structure is favored by 4.5 meV/atom over the fcc structure. Above 80 GPa, we find the fcc structure becomes stable. The fcc \rightarrow *cI16* transition occurs in our calculations

at 124 GPa. This is 20 GPa higher than seen experimentally at room temperature. We do not find Na-IV-*oP8* to be stable at any pressure. Instead, a transition of *cI16* to incommensurate Na-V occurs at 153 GPa and the *hP4* structure eventually becomes the most stable phase above 280 GPa. It is clear from Fig. 3 that the *oP8*, *tI19*, and *hP4* structures are significantly more stable at high pressures. Our calculated results are in very good agreement with previous DFT calculations by Ma *et al.* and Zhou *et al.* [16,58]. Qualitatively, the calculations thus confirm the phase sequence seen in experiments, except that, as observed previously by Ma *et al.*, the symmetry breaking of *hP4* into the *oP8* phase occurs in a region where it is unstable with respect to *cI16* and the incommensurate phase.

Two points should be noted regarding the presentation of the host-guest structure enthalpies. Firstly, in Fig. 3, we show three data sets labeled *tI19*, corresponding to the three distinct guest lattices of K-IIIa, K-IIIb, and Rb-IV—but this is not visible in the main figure, as we find the three structures to have almost equal enthalpies of formation, across the entire relevant pressure range. The inset of Fig. 3 reveals that the three possible structures are within 1 meV/atom but we find consistently, at all pressures, the K-IIIa structure to be the most stable. This structure is closest to the Na-V structure, if its monoclinic distortion is ignored (setting $\beta = 90^\circ$).

Secondly, we show in Fig. 3 the formation enthalpies at the optimal host-guest ratio. This is motivated by clear energetic differences we find between different approximants: for instance, changing the host-guest ratio in the K-IIIa structure from 1.5 (the 3g/2h structure) to 1.67 (the 5g/3h structure) results in an enthalpy gain of roughly 10 meV/atom, across the entire relevant pressure range. To visualize in more detail how sensitive the description of Na-V is to the choice of approximant, we plot in the upper panel of Fig. 4 the enthalpy against the host-guest ratio $c_H/c_G = 1.5 \dots 1.8$ for three different pressures, together with parabolic fits.

The fits work reasonably well, and the enthalpies at the respective minima for each pressure are used in Fig. 3. From Fig. 4, we can also see that the optimal host-guest ratio, the position of the enthalpy minimum, is pressure-dependent. These fitted optimal c_H/c_G ratios are shown as a function of pressure, together with two experimental data points [30], in the lower panel of Fig. 4. Based on those ground-state results, the ratio c_H/c_G should decrease monotonically with increase in pressure; while absolute numbers depend somewhat on the functional used, the same trend is found using both PBE and PBEsol. We find that the optimal host-guest ratio c_H/c_G decreases by about 1% between 140 and 200 GPa. These calculated ratios are in very good agreement with the precisely measured guest lattice at 147 GPa, but in less good agreement with the experimental data point at 130 GPa. However, note that our calculations necessitate orthorhombic guest unit cells, whereas the experimental guest lattice was found to be monoclinic.

Potassium. Calculations on relevant phases for potassium, including the incommensurate phase K-III with all three possible guest structures, were performed, and the resulting relative enthalpies are shown in Fig. 5. We reproduce the experimental stability of the bcc phase at low pressures, followed by a phase transition to fcc around 11 GPa in our calculations. At 17.5 GPa, the incommensurate phase K-III becomes more

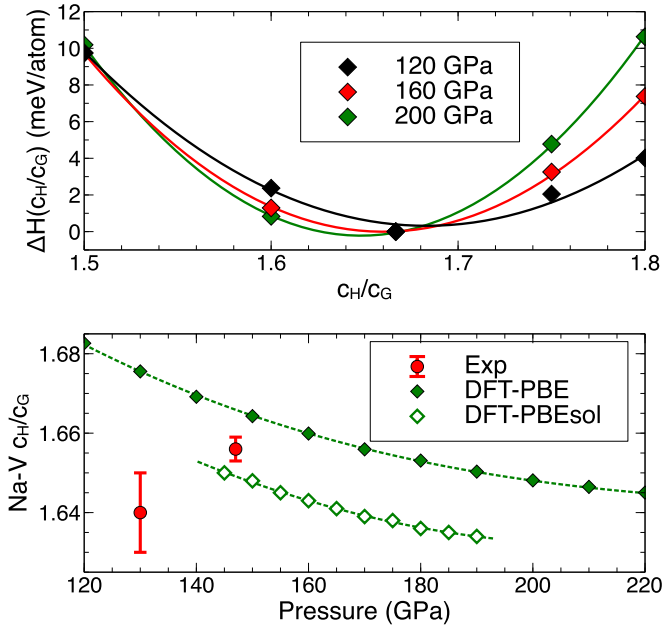


FIG. 4. Upper panel: PBE formation enthalpies of Na-V approximants (using K-IIIa guest lattice), for three pressures, and relative to the value of the 5g/3h structure ($c_H/c_G = 1.67$). Solid lines are parabolic fits. Lower panel: optimal values for c_H/c_G in Na-V as function of pressure, obtained from parabolic fits and compared to experimental data [30], from both PBE and PBEsol optimizations. Dashed lines are guides to the eye.

stable than fcc, with a very strong enthalpic driving force as pressure is increased further. Both transition pressures agree very well with experiment (11.6 and 20 GPa, respectively) [10,59]. The different guest structures are effectively degenerate in enthalpy (see inset in Fig. 5), and we will discuss their relations in more detail below. At 39 GPa in our calculations, we find the *oP8* phase to become stable (somewhat lower than its onset in experiment at 50 GPa), which in turn is followed by the *tI4* and *oC16* phases above 51 and 96 GPa, respectively (experimental transitions at 90 and 96 GPa). Overall, the phase sequence of compressed potassium is described very well, with the largest deviations being the calculated early onsets of stability of both *oP8* and *tI4*.

A more detailed insight into the energetics of the different guest lattices of K-III is given in the inset in Fig. 5. At low pressures (below 23 GPa), we find that the most stable guest structure is the primitive tetragonal structure reported by McMahon *et al.* [10] for K-IIIa. Between 23 and 38 GPa, approximant structures with a body-centered Rb-IV-type guest structure, where guest atoms in adjacent chains are offset by $c_G/2$, were found to be more stable, but by enthalpy differences of less than 0.5 meV/atom compared to the K-IIIa structure. Beyond 38 GPa, the K-IIIa structure is most stable again. We thus find, by the slimmest of energy margins, a sequence of phase transitions in the guest lattice of K-III, however, it proceeds in the order of IIIa-(Rb-IV)-IIIa, and the K-IIIb structure is not found stable under any pressure conditions in ground-state calculations. The energy differences between the different guest structures are very small, and this might explain why the stability range of the “intermediate” guest

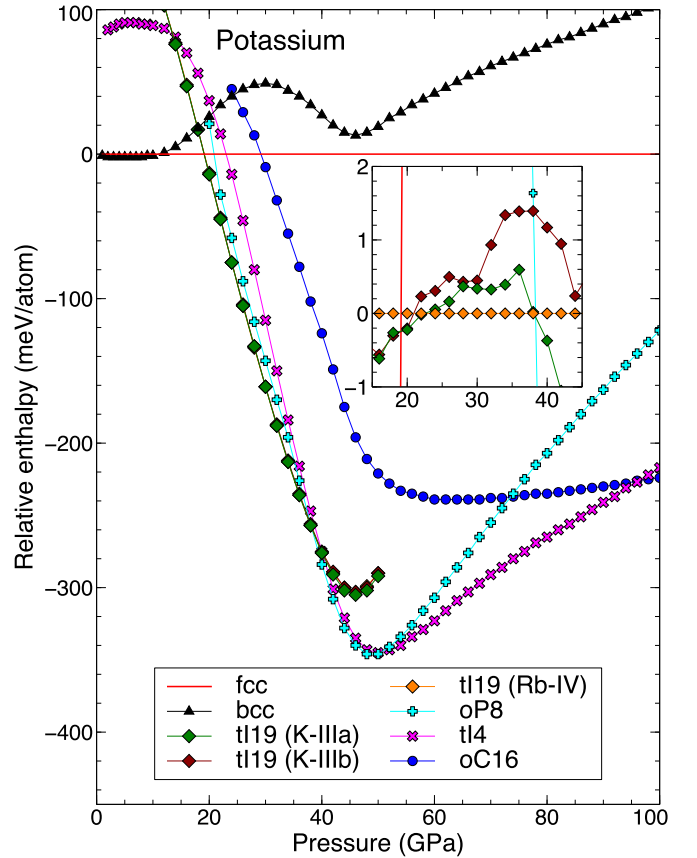


FIG. 5. PBE enthalpies of formation of various potassium structures relative to fcc as a function of pressure. The inset shows the pressure regime relevant for *tI19* formation, relative to the Rb-IV-type guest structure of *tI19*. For all *tI19* phases, the enthalpy at the optimal host-guest ratio is shown.

lattice structure (here, 23–38 GPa in the Rb-IV structure) is somewhat different from that seen in experiment, which is 30–40 GPa.

In Fig. 5, we show the enthalpy of each K-III phase at its optimal host-guest ratio. This was done, as in sodium, by using quadratic interpolations of the relative enthalpies of all approximants with $1.5 \leq c_H/c_G \leq 1.8$. Besides estimates for the optimal formation enthalpy, this procedure also gives the optimal host-guest ratio c_H/c_G as a function of pressure. As the latter has been measured quite accurately, we can compare the calculated axial ratios to the experimental data, in particular with an interest whether the approximate K-III structures can reproduce the turnaround of c_H/c_G seen in experiment [9]. The calculated optimal ratio c_H/c_G is plotted against pressure in Fig. 6. This figure also shows the data acquired by Lundegaard *et al.* Indeed, the calculations reproduce an initial decrease of c_H/c_G , with a minimum around 24 GPa (20 GPa when using the PBEsol functional), close to the calculated guest structure transition pressure, followed by a steady increase up to the highest pressures studied. Quantitatively, the optimal host-guest ratios are in excellent agreement with experimental findings, occupying the range of $c_H/c_G = 1.58$ – 1.66 in the calculated pressure range of stability. Note, however, that the calculated and measured host-guest ratio curves seem offset by

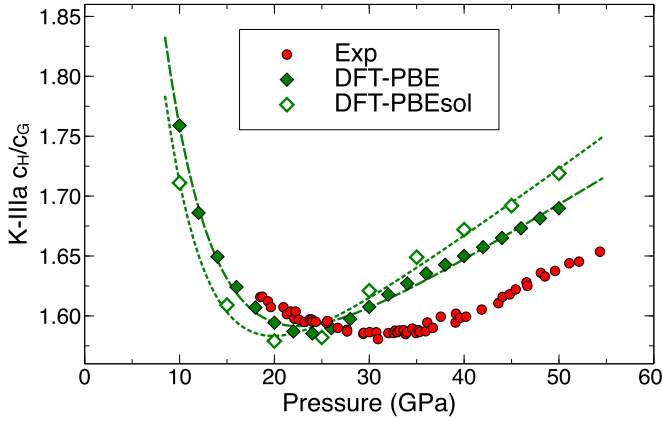


FIG. 6. Optimal c_H/c_G ratio for K-IIIa as a function of pressure, using both PBE and PBEsol. Calculated results (green diamond symbols) are from parabolic fits to approximants' data, and experimental data (red circles) are from Ref. [9]. Dashed lines are guides to the eye.

about 6–8 GPa. The reason for this is not immediately clear, but the optimal host-guest ratio is likely to be quite subtly dependent on the electronic structure or dynamic effects in the room-temperature measurements not captured in the ground state calculations.

In Fig. 7, we show experimental and computational data on the evolution of the ratio of the host lattice parameters c_H/a_H as a function of pressure. The calculated ratios depend on the choice of approximant; we show in Fig. 7 the two approximants with the most relevant host-guest ratios. For those, we find qualitative agreement with experiment, but absolute values and slopes differ quantitatively. At low pressures, before the local minimum in c_H/a_H , the host structure of K-III is more compressible along the c direction than along a .

Above 25 GPa in calculations (32 GPa in experiment [26]), the host structure experiences a significant stiffening along the c axis. Comparing the c_H/a_H axial ratio in Fig. 7 with the optimal host-guest ratio c_H/c_G in Fig. 6 allows us to study the relative compressibilities of the host and guest structures. At low pressures, when the host structure is quite compressible

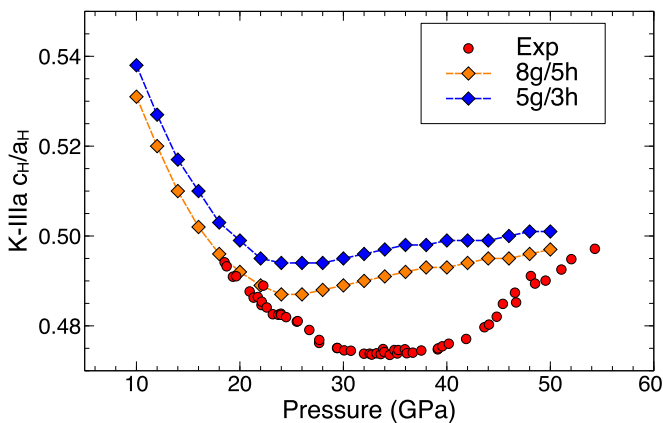


FIG. 7. K-III host lattice ratio c_H/a_H as a function of pressure, as obtained from experiment (red circles, Ref. [9]) and two relevant different approximants (orange: 8g/5h, $c_H/c_G = 1.60$; blue: 5g/3h, $c_H/c_G = 1.67$).

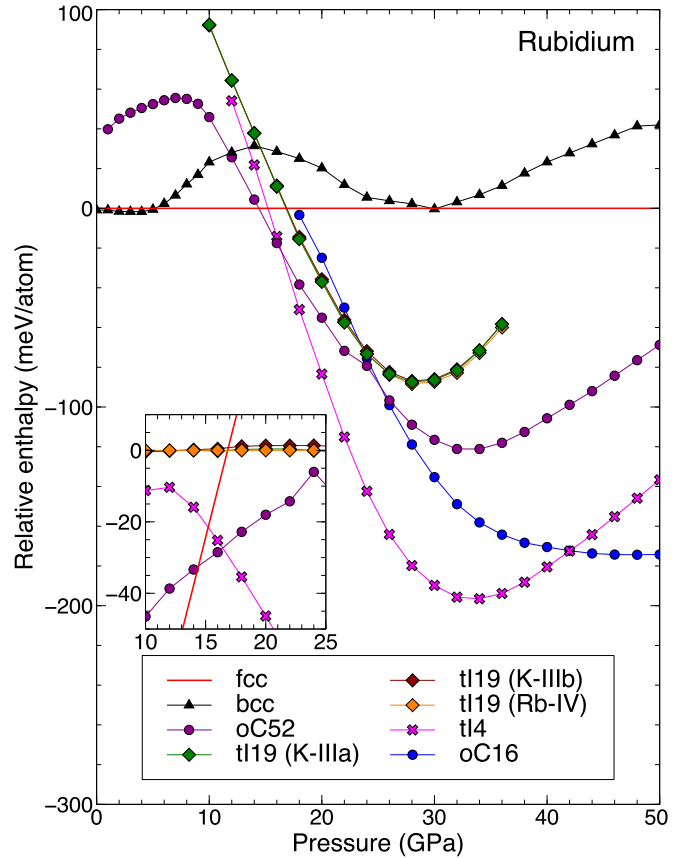


FIG. 8. PBE enthalpies of formation of various rubidium structures relative to fcc as a function of pressure. Inset shows pressure region where Rb-IV is least unstable, and relative to the Rb-IV structure. For all $tI19$ phases, the enthalpy at the optimal host-guest ratio is shown.

along the c axis, the host-guest ratio c_H/c_G also reduces. Increasing pressure thus reduces the number of guest atoms within the host structure, arguably because the guest structure is *less* compressible along c in that pressure range. Above 25 GPa in calculations, when the host structure stiffens along c , the uptake of guest atoms increases again; which is consistent with a guest structure that is *more* compressible along the c axis than the host structure at high pressure.

Rubidium. The relative formation enthalpies of relevant rubidium phases are shown in Fig. 8. The $\text{bcc} \rightarrow \text{fcc}$ transition is seen here at 6 GPa, followed by a short stability region for Rb-III ($oC52$) between 14 and 16 GPa, and the subsequent onset of Rb-V ($tI4$) is followed by Rb-VI ($oC16$) at 42 GPa. Most of these transition pressures agree very well with experiment, but our calculations fail to find a region of stability for the host-guest phase, Rb-IV, at any pressure; it is at least 30 meV/atom unstable with respect to other phases, see the inset of Fig. 8. The reason for this is not clear, but the principal applicability of DFT can probably be assumed: the same methodology that describes the stability fields of Na-V and K-III quite well (see above) should perform similarly well for Rb-IV. Calculations are for the ground state, so it is possible that Rb-IV is only stabilized by entropic effects at elevated temperatures. A recent combined experimental and computational study on

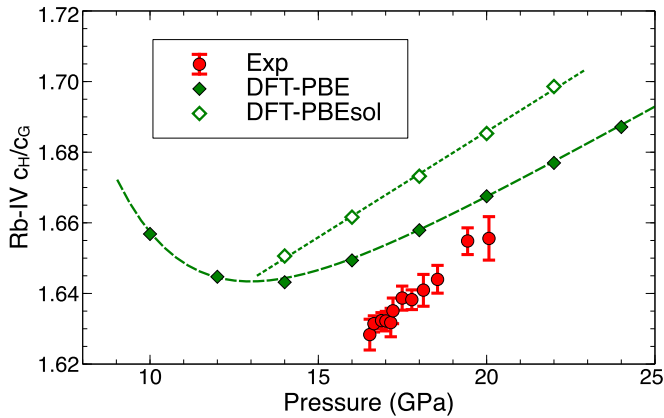


FIG. 9. Optimal c_H/c_G ratios for Rb-IV, from both PBE and PBEsol optimisations. Calculated results (green diamonds) are from parabolic fits to approximants' data, experimental data (red circles and error bars) is from Ref. [6]. Dashed lines are guides to the eye.

the high-pressure, low-temperature phase diagram of barium found indications that a new phase, Ba-VI, is more stable at low temperatures than the incommensurate host-guest phase Ba-IV [60].

Amongst the (metastable) incommensurate approximants, we find the Rb-IV guest structure to be most stable, in agreement with experiment. We then proceeded to determine, as above, the optimal host-guest ratio as a function of pressure. Figure 9 summarizes these results and shows a monotonic increase of c_H/c_G with pressure in the relevant pressure region, predicted with either of the two GGA functionals used here, and in line with experimental observations by McMahon *et al.* [6]. For both PBE and PBEsol functionals, there is an offset of the value of c_H/c_G of about 0.02–0.04 (or 4–5 GPa), while the calculated pressure gradients agree very well with the experimental result. Note that we find, with the PBE functional, a turnaround of c_H/c_G at pressures outside the stability region of Rb-IV, with a minimum at 13 GPa.

Atomic motion. For incommensurate structures, the longitudinal phonon modes of the guest and host with wave vectors along the c axis are essentially independent. This is because the forces between the guest and host atoms have an uncorrelated phase, and sum to zero. It means that there are four zero- or near-zero-frequency phonons at the Γ point, the usual three acoustic modes from the host lattice, plus a fourth mode, the phason mode, in which the guest chains slide rigidly along the chain direction relative to the host framework. At finite wave vectors along the chain direction, there are two longitudinal acoustic phonon branches: one with the periodicity of the host and the other with that of the guest [34].

Inspired by the work of Loa *et al.* [34] the guest phonon branch in Rb-IV was treated as a linear chain along the c axis. A single atom displacement allows us to find the near-neighbor spring constant k . The results are $k = 18.5 \text{ N m}^{-1}$ at 15 GPa and $k = 40 \text{ N m}^{-1}$ at 20 GPa. The speed of sound on the chain $v_g = d\sqrt{k/M}$ (where M is the mass of a Rb atom, d is the distance between them) was calculated using k and $d = c_G$. This gives $v_g = 3400 \text{ m/s}$ and 4750 m/s at 15 and 20 GPa, respectively, and $\frac{dv_g}{dP} = 270 \text{ m/sGPa}^{-1}$, which are all in good

agreement with the values obtained in the experiment by Loa *et al.* [34].

IV. ELECTRONIC STRUCTURE

We have shown that DFT is a sufficiently accurate theory to describe the stability of the incommensurate phases, but enthalpy differences do not provide any insight into the reason why nature chooses such unusual phases. We investigate several possible explanations here.

A. Electrides

Electrides form when valence electrons are displaced from the atom-centred orbitals and become localized in interstitial sites in structures such as *hP4* and *oP8* [16,27]. This is advantageous at high pressure because, while spherical objects have an optimal packing fraction of 0.74, better packing can be achieved with electrons and ions behaving as different objects. Due to the electron localization, electrides are often insulators or bad metals with large pseudogaps in the density of states (DOS) [13,16]. Typical metals are generally characterized by homogeneous profiles of valence electron density and ELF. Metals have been associated with the presence of non-nuclear maxima of the electron density but this is not a necessary requirement for a metallic system [56]. A clearer image emerges from the ELF topological approach, where a metallic system is characterized by valence ELF maxima with values not very far from that of the homogenous electron gas, low basin populations (typically much less than $1e$) and linked to other valence ELF maxima through bond interaction points with quite similar ELF values. These linkages create infinite networks of channels through the crystals that can be associated with conductivity.

Three criteria have been proposed as necessary conditions in topological analyses of molecular electrides [61]: a non-nuclear maximum (NNM) of the electron density, a valence ELF basin, and negative values of the Laplacian of the electron density. While these criteria are fulfilled in the *hP4* and *oP8* phases of Na and K, they also fit other nonelectride metallic phases. What differentiates these crystalline electride phases is the almost perfect localization of electrons in interstitial sites: the ELF maxima values are close to unity, they coincide with NNM's at the centers of the interstices, and their basins form well-defined chemical entities integrating to a pair of electrons. These Lewis pairs can be regarded as “pseudoanions,” and the crystal structures related to conventional ionic compounds where the position of these pseudoanions is occupied by anions [62].

Our topological analysis of the incommensurate alkali phases reveals a similar picture across all materials, and Fig. 10 shows typical results for Na-V (see the SM for equivalent results for K-IIIa). The distribution of the valence ELF maxima coincides with the non-nuclear maxima of the valence electron density (not shown). 2/3 of the ELF maxima (“host ELF maxima”) appear within the host network, see Figs. 10(a) and 10(b). They can be described within the same space group and lattice parameters, but number half the host atom count. The remaining ELF maxima (“channel ELF maxima”) align in chains parallel to the c axis, see Fig. 10(c), in channels provided

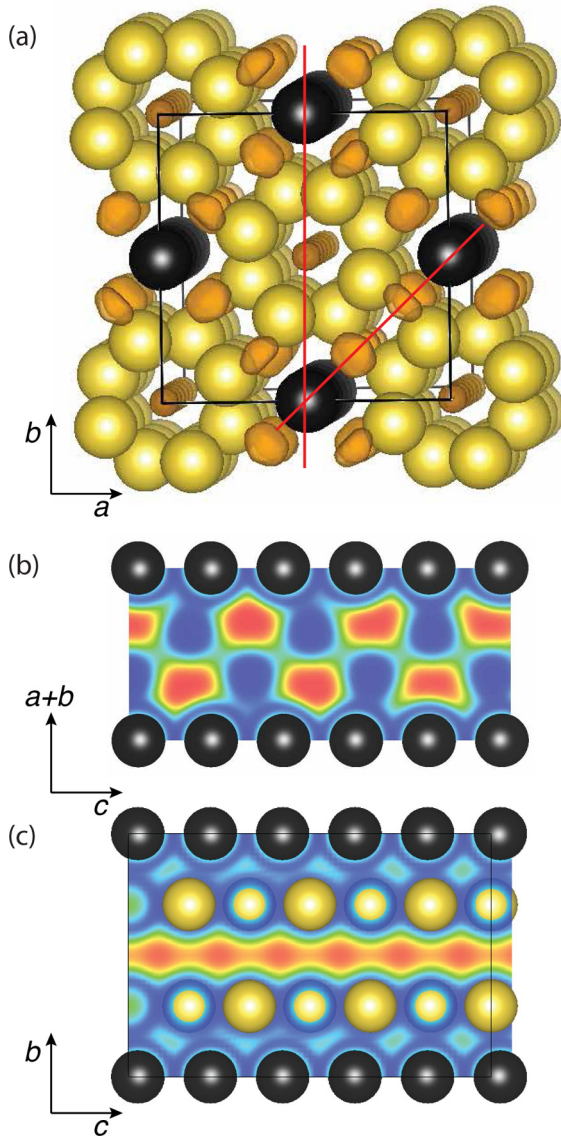


FIG. 10. ELF plots for the 5g/3h approximant of Na-V at 160 GPa, with the K-IIIa guest lattice and host/guest atoms shown as yellow/black spheres. (a) The $\text{ELF}=0.85$ isosurface in orange, seen along (001); red lines mark the positions of cross sections along $(\bar{1}10)$ and (100) shown in (b,c). These planes contain the “host” ELF maxima (b) and the “channel” ELF maxima (c). ELF values are shown from 0 (blue) to 1 (red).

by the host lattice. While their distribution corresponds to the tetragonal structure of the guest lattice in K-IIIa, they are commensurate with the *host* and not the *guest* atomic lattice along the c axis. Both types of maxima suggest high electron localization: in the 5g/3h-K-IIIa approximant of sodium at 160 GPa, their values are 0.965 (host) and 0.94 (channel), respectively. However, the ELF values at the saddle points (bond interaction points) joining the respective basins are vastly different: the ELF value at the bond interaction points between the channel ELF maxima is as high as 0.85. They should thus be seen as partially localized electrons: confined in the tetragonal plane but nearly free to move along the channels. On the other hand, the ELF values at the saddle points connecting the host ELF maxima are 0.35 on average, which we

find similar to the environment of the non-nuclear ELF maxima of the electride $hP4$ and $oP8$ phases of sodium (see Ref. [57]). Further, in analogy with those structures, the associated ELF basins have polyhedral shapes with multiple faces (10 for the K-IIIa structure) sharing boundaries with atoms. This picture explains the respective integrated electron density inside each basin, which yields approximately one electron for the channel ELF basins, but 1.69 electrons for the host ELF basins. For K and Rb the absolute numbers are lower, see Table II, but the clear difference between the host and channel basins remain: the former contain significantly more charge than the latter.

As mentioned above, charge NNM’s appear very close to the positions of the valence ELF maxima. The volumes of their corresponding basins are approximately half the size of the ELF basins and accordingly they integrate to fewer electrons, see Table II. Both host and guest atoms donate about the same number of electrons in the incommensurate phases: for sodium, using either the ELF or the QTAIM topological partitioning, partial charges on the host (guest) atoms are 0.91 (0.92) or 0.52 (0.47), respectively. This indicates that there is no chemical difference between the host and guest atoms in any of the alkali incommensurate phases.

These topological properties are qualitatively independent of the approximant used, see also the SM for the results on K-IIIa. In particular, the periodicity of the channel ELF maxima remains unaffected. Instead, choosing, e.g., a larger number of guest atoms per host unit cell simply increases the volume of the non-nuclear ELF basins and the number of electrons within them. In sodium, for instance, going from the 4g/3h approximant to the 2g/1h approximant the number of electrons within the host (channel) ELF basins changes from 1.63 to 1.77 (0.97 to 1.09).

We therefore conclude that the electride character of the incommensurate phases is (i) mainly governed by the host structure, and (ii) comprises two qualitatively different contributions—fully localized ELF basins whose electron density integration tends to one pair of electrons each, and a 1D distribution of partially localized electrons along channels in the host structure. The role of the guest atoms therefore seems to be to contribute further electronic charge, while occupying a second set of channels inside the host lattice (a necessity for stable packing at high pressures).

We performed two additional simulations on sodium to corroborate these conclusions. Firstly, we analyzed the empty host structure (removing all guest atoms), and secondly we substituted the guest atoms by chemically inert Ne atoms, the noble gas closest to sodium in the periodic table. In either case, the qualitative topology of the non-nuclear ELF maxima does not change: both the host and channel ELF maxima remain present and located at approximately the same positions. Moreover, the volumes and integrated number of electrons within the channel ELF basins remains almost identical. The reduction of the number of atoms/electrons in both hypothetical systems thus only affects the number of electrons within the host ELF basins, as well as their volumes and shapes. In particular, in the empty host structure, the host ELF basin volume increases by 13.7%, but integrates to only 1.32 electrons as a consequence of the smaller total number of sodium atoms donating electrons. When using Ne guest atoms, their volume decreases by 15.8% due to the bigger volume of

TABLE II. Electronic charges n integrated over the non-nuclear “host” and “channel” basins as well as partial charges q of the host and guest atoms, devised from both ELF and charge (QTAIM) topologies, for relevant approximants of Na, K, and Rb.

	Pressure	Structure	ELF basins				Charge basins			
			n_{host}	n_{channel}	q_{host}	q_{guest}	n_{host}	n_{channel}	q_{host}	q_{guest}
Na	160 GPa	5g/3h-K-IIIa	1.69	1.04	+0.91	+0.92	0.94	0.58	+0.52	+0.47
K	40 GPa	5g/3h-K-IIIa	1.16	0.72	+0.63	+0.64	0.41	0.22	+0.22	+0.17
Rb	20 GPa	8g/5h-Rb-IV	1.22	0.77	+0.66	+0.68	0.37	0.21	+0.20	+0.15

the Ne atoms, yet they integrate to 1.29 electrons (the Ne atoms do not contribute to the electron donation).

In the spirit of interpreting electride phases as “pseudobinary” ionic compounds, one can relate the alkali incommensurate phases to the W_5Si_3 structure type [33,63,64]. There, the metal cations occupy the same sites as the alkali host and guest atoms, with a nominal host-guest ratio of $c_H/c_G = 2.0$, while the electronegative silicon atoms occupy the same sites as the “host” and “channel” ELF and charge maxima. The W_5Si_3 structure has very short W-W separations along the “guest chains”, and it has been proposed that these sites should be partially occupied, possibly favoring the formation of incommensurate phases at ambient pressure conditions [65]. This seems to be the case in several ternary intermetallic alloys with this structure, as well as the $\text{Ba}_{4.81}\text{Pb}_3$ compound [65,66]. The latter would have a host-guest ratio of 1.62, very close to the value seen in the alkali incommensurate phases.

B. s - d transfer or hybridization

One argument for the appearance of complex structures is that there is either s - d transfer or sd hybridization. The argument runs that the d orbital is smaller and favored at high pressure and thus, because it has a complex shape, symmetry breaking is induced. The discovery of complex phases in lithium and sodium means that the original s - d argument must be generalized to incorporate s - p interactions.

We tested this hypothesis via examination of the partial density of states, obtained as projections onto s , p , and d orbitals within the PAW spheres at each atomic site. In Fig. 11, we show these projections, integrated over all occupied states, as a function of pressure for the fcc, incommensurate host, incommensurate guest, and $tI4$ structures in Na, K, and Rb, respectively. Firstly, note that these projections pick up the filled $(n-1)s^2$ and $(n-1)p^6$ valence shells of all elements, and so the numbers of s and p electrons hover around 2 and

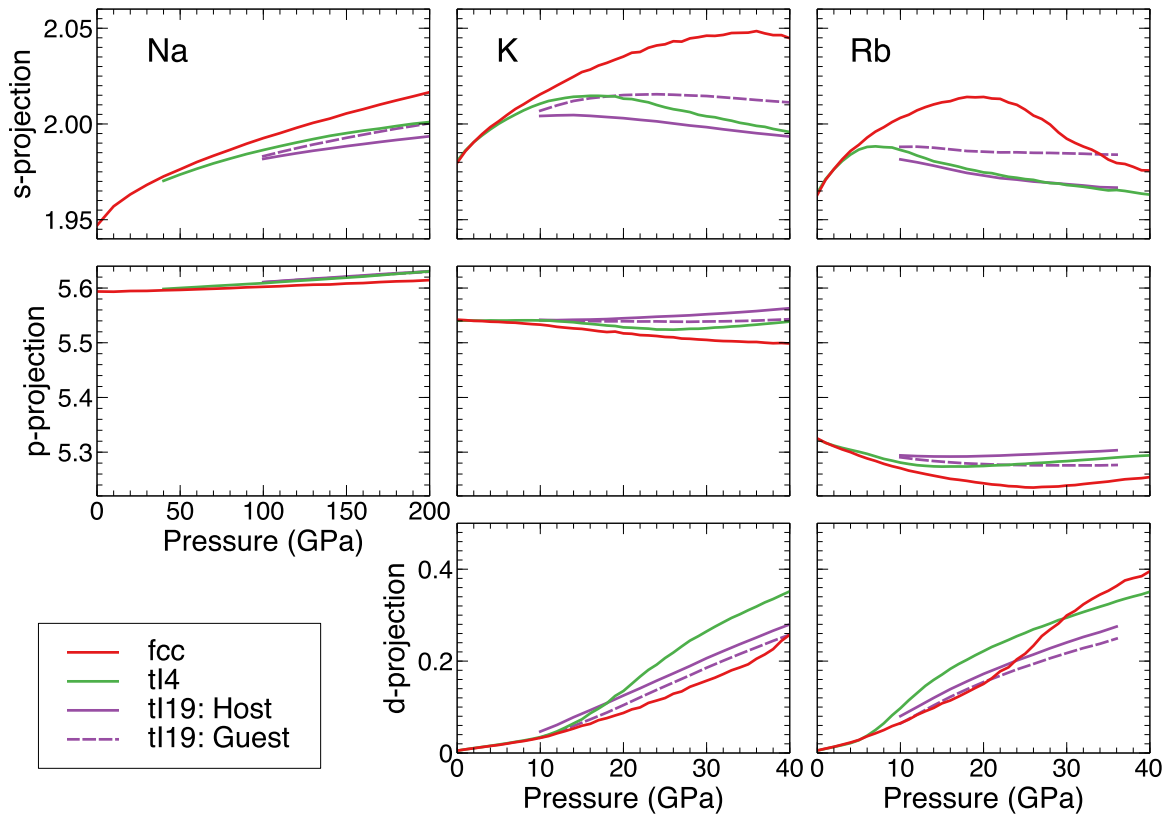


FIG. 11. Projection of the electronic wave functions onto localized s , p , and d orbitals for three different structures of Na, K, and Rb. The exact magnitude of the projection depends on the precise definition of the localized orbitals, hence the method counts slightly fewer than six semicore p electrons. Within uncertainty, the data implies that projected densities are independent of crystal structure.

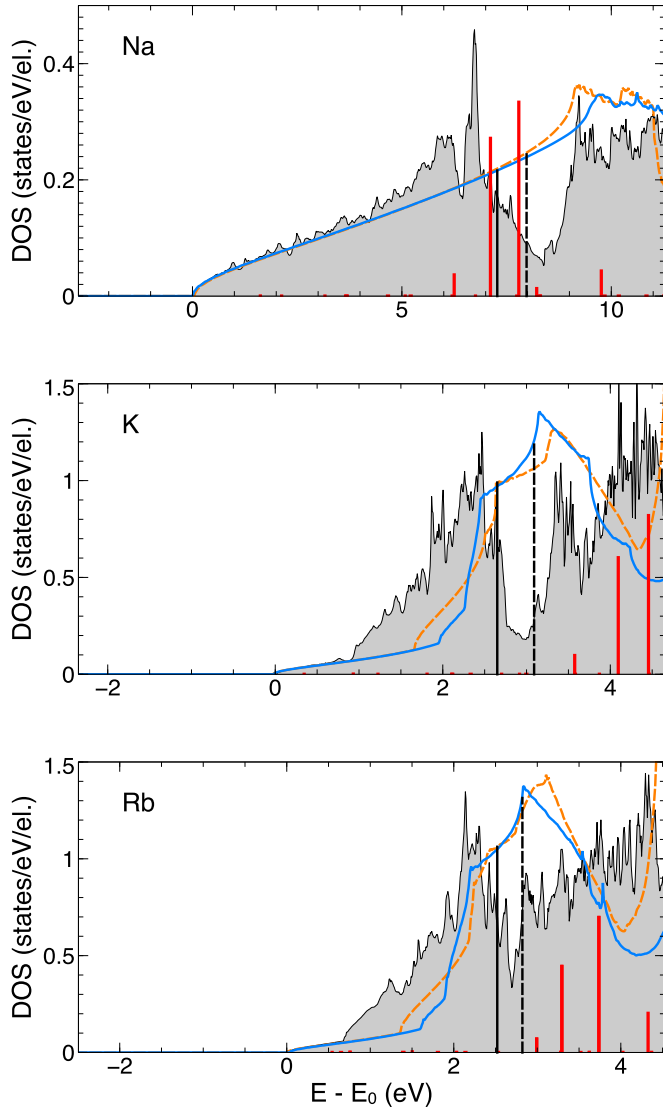


FIG. 12. From top to bottom: electronic DOS for Na (8g/5h, 160 GPa), K (8g/5h, 30 GPa), and Rb (5g/3h, 20 GPa) as grey shaded areas, with their Fermi energies (black solid lines). Also shown are the DOS of bcc/fcc phases at the same valence electron densities (blue/orange lines) with their Fermi energies (black dashed lines), and the diffraction peaks of the incommensurate structures (solid red bars) as a function of wave vector k expressed as $E(k) = \hbar^2 k^2 / 2m_e$. All energies are normalized to coincide with the valence band onset of the incommensurate phases.

6, respectively. Increasing pressure results for Na in a small increase of p occupancy but for K and Rb in much more pronounced increases of the d occupancies. The differences between structures, and between the host and guest atoms of the incommensurate phases, are very small. The s occupancies in all high-pressure phases (i.e., except fcc) remain largely constant. This independence of crystal structure indicates hybridization rather than electron transfer; the latter would be expected to show a stronger dependence on the atomic arrangement. The data also suggest that the electronic structure of compressed Na is different from K and Rb: while for Na there seems to be no discernible s - p transfer or localization of quasifree electrons, the population of K and Rb d states

is significant. The d concentration depends on pressure rather than structure, indicating that s - d transfer does not play a role in stabilizing the incommensurate phases.

C. Fermi surface effects

Another mechanism proposed for the high pressure phases is known as Brillouin-zone/Fermi-surface effect, variously described through the concepts of Jones zones, Hume-Rothery rules, charge density waves, Peierls distortion or Fermi-surface nesting [19,25,67]. It involves the lowering of the energy due to perturbation of electronic states at the Fermi surface by the lattice structure. In some cases, the effect may induce soft phonons or Kohn anomalies. This effect scales proportionally with the density [19], more rapidly than Coulomb or kinetic energy terms, so at high pressures the entire structure may be dominated by this effect. DFT calculations cannot be directly written as a perturbation on a free electron gas, but the effect can be determined by the presence of reciprocal lattice vectors close to $2k_F$, where k_F is the Fermi wave vector. A particularly good example is the $cI16$ structure, which is a distortion of bcc that produces strong diffraction at $(1, \frac{1}{2}, \frac{1}{2})_{bcc}$, which lies at the Fermi surface for monatomic bcc metals [68].

For the alkali $tI19$ structures, electronic DOS's for reasonable approximants at relevant pressures are shown in Fig. 12, together with the DOS's of simple bcc and fcc structures at the same respective valence electron densities, and simulated diffraction patterns for the incommensurates drawn as a function of k^2 . All incommensurates have narrower electronic bandwidths than the simple phases, which alludes to partial localization of electronic charge (see electrone discussion above), however, there seems a qualitative difference between Na and K/Rb. The Na- $tI19$ DOS suggests a straightforward distortion from the free electron gas: dominant diffraction peaks of the $tI19$ structure (the [211] and [310] reflections of the host lattice) are just below the Fermi energy of bcc and fcc, and the structural transition to the $tI19$ phase shifts spectral weight to lower energies, establishes a pseudogap (not at all present in bcc or fcc), and lowers the Fermi energy. For K and Rb, instead, the s - d hybridization discussed above (or rather, the localization of quasifree electrons into d orbitals) means much narrower valence bands, independent of the crystal structure, and the DOSs look very different from that of the homogeneous electron gas. For both elements, significant pseudogaps in the $tI19$ phase lead to electronic stabilization over the simple crystal structures and a lowering of the Fermi energy. However, note that the diffraction peaks of $tI19$ are at energies quite far above the Fermi energy, and the simple perturbative approach of Brillouin zone effects does not apply to either element. Since their electronic structure, with its significant d -orbital character, is quite far removed from the homogeneous electron gas, that is perhaps not surprising.

V. CONCLUSIONS

We have investigated here the ability of DFT to accurately describe the incommensurate phases of Na, K, and Rb, focusing on subtle effects such as details of the guest lattice and pressure-dependence of the guest content. The structures were modeled using a series of commensurate approximants, which

allows us to predict a continuous variation in the c_H/c_G ratio as a function of pressure. Na-V (neglecting monoclinic guest lattice distortions) was found to be stable between 153 and 280 GPa with the K-IIIa guest lattice. We predict a monotonic decrease of c_H/c_G with increased pressure. K-III was found to be stable in the pressure range 17.5–39 GPa. Calculated c_H/c_G and c_H/a_H ratios and their respective pressure dependencies agree with observed values [9]. In particular, calculations can reproduce a local minimum of c_H/c_G within the stability range of the incommensurate phase. This minimum appears independent of the phase transition between K-IIIa and K-IIIb. In fact, while calculations confirm that the guest lattice of K-III undergoes a reentrant phase transition, we find the sequence IIIa–Rb-IV–IIIa. For rubidium, the Rb-IV guest lattice was confirmed as most stable, and the calculated c_H/c_G ratio was found to reproduce the experimentally-seen monotonic increase, with a gradient of 0.0060 GPa^{-1} [6]. Rb-IV was, however, found to be unstable across its expected stability range compared with the Rb-III and Rb-V phases. Rb-V, with the $tI4$ structure, also appeared abnormally stabilized with respect to Rb-III. The reason behind this has not been deduced, and further investigation is required; note that K-V (which has the $tI4$ structure) also seems too stable with respect to K-IV, but does not qualitatively influence the phase sequence. It is also conceivable that Rb-IV is a high-temperature phase and not the true ground state in the relevant pressure range, similar to what has been reported recently in the barium phase diagram [60]. Dynamical properties of the Rb guest lattice reproduce the experimental sound velocity measurements very well.

The incommensurate phases all show an interesting pattern of electron localization, which we find to emerge from the host structure alone. It features truly localized pairs of electrons in the host network as well as host-modulated 1D chains along the c axis. The number of electrons localized in these

chains is only a fraction of the total valence electron count, and incommensurate phases should be seen as intermediate states towards “true” electride phases such as $oP8$ and $hP4$ that appear as competing phases at similar compressions. The charge localization is independent of the presence or absence of the guest atoms. However, the latter contribute to the high density necessary for a high-pressure phase, and generally boost the electridelike character by donating more electrons to the interstitial maxima. All incommensurate alkali phases feature prominent pseudogaps and reduced bandwidths in the electronic DOS, but seem not universally stabilized by Fermi surface-Brillouin zone effects. Na-V fits this explanation, with relatively small deviations of the electronic structure from the homogeneous electron gas, and diffraction peaks of the $tI19$ phase that can establish a pseudogap around the Fermi energy. Both K-III and Rb-IV, however, show significant d -orbital character of the valence electrons, which we interpret as hybridization, as pressure increases. Note that there is no significant difference in the amount of hybridization between competing crystal structures. While both K-III and Rb-IV exhibit significant pseudogaps (in contrast to simple bcc and fcc), these are not caused by Fermi surface-Brillouin zone interactions. We conclude that hybridization is important under compression, but not for determining the crystal structure.

ACKNOWLEDGMENTS

G.J.A. acknowledges support from a Royal Society Wolfson award, and M.M. and G.J.A. the ERC grant Hecate. G.W. and V.N.R. thank EPSRC CM-CDT Grant No. EP/L015110/1 for studentships. Computing resources were provided by EPSRC via the UKCP consortium (Grant No. EP/P022790/1). Data from the calculations are accessible on the University of Edinburgh’s Datashare repository at <http://datashare.is.ed.ac.uk/>.

- [1] I. Loa, R. J. Nelmes, L. F. Lundegaard, and M. I. McMahon, *Nat. Mater.* **11**, 627 (2012).
- [2] M. I. McMahon, T. Bovornratanarak, D. R. Allan, S. A. Belmonte, and R. J. Nelmes, *Phys. Rev. B* **61**, 3135 (2000).
- [3] H. Fujihisa, Y. Nakamoto, M. Sakata, K. Shimizu, T. Matsuoka, Y. Ohishi, H. Yamawaki, S. Takeya, and Y. Gotoh, *Phys. Rev. Lett.* **110**, 235501 (2013).
- [4] M. I. McMahon and G. J. Ackland, *Nat. Mater.* **9**, 607 (2010).
- [5] M. Marqués, G. J. Ackland, L. F. Lundegaard, G. Stinton, R. J. Nelmes, M. I. McMahon, and J. Contreras-García, *Phys. Rev. Lett.* **103**, 115501 (2009).
- [6] M. I. McMahon, S. Rekhi, and R. J. Nelmes, *Phys. Rev. Lett.* **87**, 055501 (2001).
- [7] S. Falconi, M. I. McMahon, L. F. Lundegaard, C. Hejny, R. J. Nelmes, and M. Hanfland, *Phys. Rev. B* **73**, 214102 (2006).
- [8] M. I. McMahon and R. J. Nelmes, *Phys. Rev. Lett.* **93**, 055501 (2004).
- [9] L. F. Lundegaard, G. W. Stinton, M. Zelazny, C. L. Guillaume, J. E. Proctor, I. Loa, E. Gregoryanz, R. J. Nelmes, and M. I. McMahon, *Phys. Rev. B* **88**, 054106 (2013).
- [10] M. I. McMahon, R. J. Nelmes, U. Schwarz, and K. Syassen, *Phys. Rev. B* **74**, 140102 (2006).
- [11] M. I. McMahon, E. Gregoryanz, L. F. Lundegaard, I. Loa, C. Guillaume, R. J. Nelmes, A. K. Kleppe, M. Amboage, H. Wilhelm, and A. P. Jephcoat, *Proc. Natl. Acad. Sci. USA* **104**, 17297 (2007).
- [12] I. Loa, K. Syassen, G. Monaco, G. Vankó, M. Krisch, and M. Hanfland, *Phys. Rev. Lett.* **107**, 086402 (2011).
- [13] M. Marqués, M. I. McMahon, E. Gregoryanz, M. Hanfland, C. L. Guillaume, C. J. Pickard, G. J. Ackland, and R. J. Nelmes, *Phys. Rev. Lett.* **106**, 095502 (2011).
- [14] M. Hanfland, I. Loa, and K. Syassen, *Phys. Rev. B* **65**, 184109 (2002).
- [15] A. Lazicki, A. F. Goncharov, V. V. Struzhkin, R. E. Cohen, Z. Liu, E. Gregoryanz, C. Guillaume, H.-K. Mao, and R. J. Hemley, *Proc. Natl. Acad. Sci. USA* **106**, 6525 (2009).
- [16] Y. Ma, M. Eremets, A. R. Oganov, Y. Xie, I. Trojan, S. Medvedev, A. O. Lyakhov, M. Valle, and V. Prakapenka, *Nature (London)* **458**, 182 (2009).
- [17] P. K. Ahluwalia, S. J. Clark, and G. J. Ackland, in *Solid State Physics: Proceedings of the DAE Solid State Physics Symposium* (Universities Press (India), Hyderabad, 1998), Vol. 41, p. 147.
- [18] V. Heine, *Nature (London)* **403**, 836 (2000).

- [19] G. J. Ackland and I. R. MacLeod, *New J. Phys.* **6**, 138 (2004).
- [20] O. Degtyareva, *High Press. Res.* **30**, 343 (2010).
- [21] J. B. Neaton and N. W. Ashcroft, *Nature (London)* **400**, 141 (1999).
- [22] J. Sun, S. Lee, and J. Lin, *Chem. - An Asian J.* **2**, 1204 (2007).
- [23] U. Häussermann, K. Söderberg, and R. Norrestam, *J. Am. Chem. Soc.* **124**, 15359 (2002).
- [24] H. Jones, *The Theory of Brillouin Zones and Electron States in Crystals* (North Holland, Amsterdam, 1962).
- [25] V. F. Degtyareva, *J. Phys.: Conf. Ser.* **653**, 012075 (2015).
- [26] E. E. McBride, K. A. Munro, G. W. Stinton, R. J. Husband, R. Briggs, H. P. Liermann, and M. I. McMahon, *Phys. Rev. B* **91**, 144111 (2015).
- [27] M. Marqués, M. Santoro, C. L. Guillaume, F. A. Gorelli, J. Contreras-García, R. T. Howie, A. F. Goncharov, and E. Gregoryanz, *Phys. Rev. B* **83**, 184106 (2011).
- [28] E. Gregoryanz, L. F. Lundegaard, M. I. McMahon, C. Guillaume, R. J. Nelmes, and M. Mezouar, *Science* **320**, 1054 (2008).
- [29] B. Rousseau, Y. Xie, Y. Ma, and A. Bergara, *Eur. Phys. J. B* **81**, 1 (2011).
- [30] L. F. Lundegaard, E. Gregoryanz, M. I. McMahon, C. Guillaume, I. Loa, and R. J. Nelmes, *Phys. Rev. B* **79**, 064105 (2009).
- [31] C. J. Pickard and R. J. Needs, *J. Phys.: Condens. Matter* **23**, 053201 (2011).
- [32] L. F. Lundegaard, M. Marqués, G. Stinton, G. J. Ackland, R. J. Nelmes, and M. I. McMahon, *Phys. Rev. B* **80**, 020101 (2009).
- [33] U. Schwarz, A. Grzechnik, K. Syassen, I. Loa, and M. Hanfland, *Phys. Rev. Lett.* **83**, 4085 (1999).
- [34] I. Loa, L. F. Lundegaard, M. I. McMahon, S. R. Evans, A. Bossak, and M. Krisch, *Phys. Rev. Lett.* **99**, 035501 (2007).
- [35] A. N. Kolmogorov and S. Curtarolo, *Phys. Rev. B* **74**, 224507 (2006).
- [36] S. Arapan, H.-k. Mao, and R. Ahuja, *Proc. Natl. Acad. Sci. USA* **105**, 20627 (2008).
- [37] S. Arapan, N. V. Skorodumova, and R. Ahuja, *Phys. Rev. Lett.* **102**, 085701 (2009).
- [38] A. Hermann, A. Suarez-Alcubilla, I. G. Gurtubay, L.-M. Yang, A. Bergara, N. W. Ashcroft, and R. Hoffmann, *Phys. Rev. B* **86**, 144110 (2012).
- [39] A. Hermann, A. McSorley, N. W. Ashcroft, and R. Hoffmann, *J. Am. Chem. Soc.* **134**, 18606 (2012).
- [40] S. J. Clark, M. D. Segall, C. J. Pickard, P. J. Hasnip, M. I. J. Probert, K. Refson, and M. C. Payne, *Z. Krist.-Cryst. Mater.* **220**, 567 (2005).
- [41] G. I. Csonka, J. P. Perdew, A. Ruzsinszky, P. H. T. Philipsen, S. Lebègue, J. Paier, O. A. Vydrov, and J. G. Ángyán, *Phys. Rev. B* **79**, 155107 (2009).
- [42] J. P. Perdew, K. Burke, and M. Ernzerhof, *Phys. Rev. Lett.* **77**, 3865 (1996).
- [43] L. He, F. Liu, G. Hautier, M. J. T. Oliveira, M. A. L. Marques, F. D. Vila, J. J. Rehr, G.-M. Rignanese, and A. Zhou, *Phys. Rev. B* **89**, 064305 (2014).
- [44] B. G. Pfrommer, M. Côté, S. G. Louie, and M. L. Cohen, *J. Comput. Phys.* **131**, 233 (1997).
- [45] D. Vanderbilt, *Phys. Rev. B* **41**, 7892 (1990).
- [46] Inorganic Crystal Structure Database (ICSD), <https://icsd.fiz-karlsruhe.de/search/index.xhtml>, accessed: Sep 2015.
- [47] C. F. Guerra, J.-W. Handgraaf, E. J. Baerends, and F. M. Bickelhaupt, *J. Comp. Chem.* **25**, 189 (2004).
- [48] M. D. Segall, R. Shah, C. J. Pickard, and M. C. Payne, *Phys. Rev. B* **54**, 16317 (1996).
- [49] A. D. Becke and K. E. Edgecombe, *J. Chem. Phys.* **92**, 5397 (1990).
- [50] A. Savin, O. Jepsen, J. Flad, O. K. Andersen, H. Preuss, and H. G. von Schnering, *Angew. Chemie Int. Ed.* **31**, 187 (1992).
- [51] A. Otero-de-la Roza, E. R. Johnson, and V. Luaña, *Comput. Phys. Commun.* **185**, 1007 (2014).
- [52] G. Kresse and J. Furthmüller, *Phys. Rev. B* **54**, 11169 (1996).
- [53] G. Kresse and D. Joubert, *Phys. Rev. B* **59**, 1758 (1999).
- [54] R. F. W. Bader, *Atoms in Molecules: A Quantum Theory* (Oxford University Press, Oxford, UK, 1994).
- [55] W. Tang, E. Sanville, and G. Henkelman, *J. Phys.: Condens. Matter* **21**, 084204 (2009).
- [56] B. Silvi and C. Gatti, *J. Phys. Chem. A* **104**, 947 (2000).
- [57] See Supplemental Material at <http://link.aps.org/supplemental/10.1103/PhysRevMaterials.2.053604> for crystal structures and extended ELF analysis.
- [58] D. W. Zhou, G. Bao, Y. M. Ma, T. Cui, B. B. Liu, and G. T. Zou, *J. Phys.: Condens. Matter* **21**, 025508 (2009).
- [59] H. Olijnyk and W. B. Holzapfel, *Phys. Lett. A* **99**, 381 (1983).
- [60] S. Desgreniers, J. S. Tse, T. Matsuoka, Y. Ohishi, Q. Li, and Y. Ma, *Appl. Phys. Lett.* **107**, 221908 (2015).
- [61] V. Postils, M. Garcia-Borràs, M. Solà, J. M. Luis, and E. Matito, *Chem. Commun.* **51**, 4865 (2015).
- [62] M.-S. Miao and R. Hoffmann, *Acc. Chem. Res.* **47**, 1311 (2014).
- [63] B. Aronsson, *Acta Chem. Scand.* **9**, 1107 (1955).
- [64] E. Parthé, H. Nowotny, and H. Schmid, *Monatshefte für Chemie* **86**, 385 (1955).
- [65] A. K. Ganguli, S. Gupta, J. T. Zhao, E. Alejandro Leon-Escamilla, and J. D. Corbett, *J. Solid State Chem.* **178**, 2959 (2005).
- [66] I. Schewe-Miller and P. Böttcher, *J. Alloys Compd.* **183**, 98 (1992).
- [67] V. F. Degtyareva, *High Press. Res.* **23**, 253 (2003).
- [68] M. Hanfland, K. Syassen, N. E. Christensen, and D. L. Novikov, *Nature (London)* **408**, 174 (2000).